

Solar-Electric and Gas Powered, Long-Endurance UAV Sizing via Geometric Programming

Michael Burton^{*} and Warren Hoburg[†]

Massachusetts Institute of Technology, Cambridge, 02139, USA

Fueled by telecommunication needs and opportunities, there has been a recent push to develop aircraft that can provide long-endurance (days to weeks) persistent aerial coverage. These aircraft present a complicated systems engineering problem because of the multifaceted interaction of various requirements, such as endurance, wind speeds, operational capability and coverage footprint. In this paper, a comparison of solar-electric and gas powered, long-endurance aircraft is accomplished. Geometric programming, a form of convex optimization, can reliably solve problems with thousands of variables in seconds and is used as an optimization tool to evaluate the design trade offs between architectures and requirements. The results show that long-endurance, gas powered aircraft are generally more robust to higher wind speeds than solar-powered aircraft. However, gas powered aircraft are limited in their endurance by the amount of fuel that they can carry. While solar-electric powered aircraft can theoretically fly for months, they are operationally limited by reduced solar flux during the winter and wind speeds at higher latitudes. Using geometric programming, a detailed trade study between gas-powered and solar-powered aircraft is performed to discover which architecture is best suited to meet a given set of requirements, and what is the optimum size and endurance of that platform.

Nomenclature

A	wing aspect ratio	$(E/S)_{\text{day}}$	daily required solar energy
\bar{A}	non-dimensional cross sectional area	$(E/S)_{\text{sun}}$	available solar energy
b	wing span	f_{solar}	planform area fraction covered in solar cells
BSFC	brake specific fuel consumption	$f_{\text{structural}}$	fractional structural weight
BSFC _{100%}	BSFC at full throttle	g	gravitational constant
c	wing chord	h	flight altitude
C_D	aircraft drag coefficient	\dot{h}_{min}	minimum climb rate
C_{d0}	non-wing drag coefficient	h_{batt}	battery specific energy
c_{d_p}	wing profile drag coefficient	h_{cap}	spar cap separation
C_f	skin friction coefficient	I	cap spar moment of inertia
C_L	lift coefficient	I_0	tail boom root moment of inertia
c_{l_α}	lift slope coefficient	k	tail boom taper index
$C_{L_{\text{max}}}$	maximum lift coefficient	K_q	wing loading constant
d	tail boom diameter	L_h	horizontal tail lift
D_{boom}	tail boom drag	l_{fuse}	fuselage length
ΔW	wing section weight	l_h	horizontal tail moment arm
Δy	wing section length	l_v	vertical tail moment arm
DOY	day of the year	m	tail boom mass
e	span efficiency factor	m'	local wing mass
E	Young's Modulus	m_{fac}	weight margin factor
E_{batt}	energy stored in battery	m_{motor}	electric motor mass
E_{sun}	total solar energy available	\dot{m}_{fuel}	fuel flow rate
$(E/S)_{\text{twilight}}$	twilight solar energy	\mathcal{M}	wing bending moment

^{*}Master's Candidate, Aeronautics and Astronautics Engineering, 77 Mass Ave, Cambridge MA, 02139, AIAA Student.

[†]Assistant Professor, Aeronautics and Astronautics Engineering, 77 Mass Ave, Cambridge MA, 02139, AIAA Member.

n	number of wing segments	W_{batt}	battery weight
N	number of flight segments	w_{cap}	spar cap width
N_{max}	safety load factor	W_{cent}	center of aircraft weight
p_{wind}	percentile wind speed	W_{emp}	empennage weight
P_0	magnitude of available solar power	W_{engine}	engine weight
P_{avionics}	avionics power	W_{fadd}	additional wing structural weight
P_{oper}	aircraft operating power	W_{final}	end of flight segment aircraft weight
$(P/S)_{\text{min}}$	minimum operational solar power	W_{fuel}	fuel weight
P_{shaft}	engine/motor shaft power	W_{fuselage}	fuselage weight
P_{sun}	useable solar power per unit area	W_{h}	horizontal tail weight
$P_{\text{sun surface}}$	power emitted at the sun's surface	W_{initial}	start of flight segment aircraft weight
r_0	average distance from earth to sun	w_{max}	maximum deflection limit
R	aircraft range	W_{MTO}	max take-off weight
$R_{\text{earth orbit}}$	distance from earth to sun	W_{payload}	payload weight
R_{fuse}	fuselage radius	W_{skin}	wing skin weight
R_{spec}	specific gas constant	W_{solar}	solar cell weight
R_{sun}	radius of the sun	W_{spar}	wing spar weight
q	distributed wing loading	$W_{\text{structural}}$	structural weight
\bar{q}	normalized distributed wing loading	W_{v}	vertical tail weight
Re	aircraft Reynolds number	W_{wing}	wing weight
Re_{boom}	tail boom Reynolds number	y	distance from wing root along span
S	wing planform area	z_{bre}	Breguet Range helper variable
\mathcal{S}	shear force	α	angle of attack
S_{fuse}	fuselage wetted surface area	α_{gust}	local angle of attack from gust velocities
S_{h}	horizontal tail planform area	Δ	solar declination angle
S_{solar}	solar cell area	η_{charge}	battery charging efficiency
S_{v}	vertical tail planform area	$\eta_{\text{discharge}}$	battery discharging efficiency
t	flight time	η_{motor}	electric motor efficiency
t_0	tail boom root wall thickness	η_{prop}	propulsive efficiency
t_{cap}	spar cap thickness	η_{solar}	solar cell efficiency
t_{day}	hours of daylight	ϕ	latitude
t_{night}	hours of darkness	ρ	air density
$t_{\text{sun rise}}$	time of sun rise	ρ_{Acfpr}	area density of carbon fiber
$t_{\text{sun set}}$	time of sun set	ρ_{cfpr}	density of carbon fiber
T	aircraft thrust	ρ_{foam}	density of foam
V	true airspeed	ρ_{solar}	solar cell density
V_{fuse}	fuselage volume	σ_{cfpr}	maximum carbon fiber stress
V_{gust}	gust velocity	τ_{h}	horizontal tail thickness to chord ratio
V_{h}	horizontal tail lift coefficient	τ_{t}	wing thickness to chord ratio
V_{ref}	reference wind airspeed	τ_{v}	vertical tail thickness to chord ratio
V_{wind}	wind speed	τ_{w}	cap spar width to chord ratio
V_{v}	vertical tail lift coefficient	θ	angle normal to surface
w	wing deflection	θ_{boom}	tail boom deflection angle
W	aircraft weight	Θ	wing bending deflection angle
W_{ave}	average weight over a flight segment		

I. Introduction

Long-endurance station-keeping aircraft are potential solutions to providing internet, communication, and persistent surveillance. Recently, tech companies such as Google[1] and Facebook[2] have explored the possibility of using solar-electric powered aircraft to provide internet to parts of the world where 4G or 3G network is not available. Engineering firms like Aurora Flight Sciences[3] and Vanilla Aircraft[4] have developed gas powered long-endurance platforms as a means of providing continual surveillance for days at a time. Sizing of such long-endurance aircraft is complicated because of the multifaceted interaction between aerodynamics, structural weight, solar energy, wind speed, and other disciplines and environmental models. The complexity of sizing these kinds of aircraft makes the trade offs between gas powered and solar-powered architectures potentially non-intuitive.

This paper presents a physics-based optimization model that uses geometric programming as a systematic and rapid approach to evaluate trade offs between the two architectures for a given mission. Geometric

programming, a form of convex optimization, is chosen as a means of evaluating the design space because of its rapid solve time and guaranteed convergence to a global optimum.[5] Models and equations representing the interaction of the various disciplines are expressed in a geometric programming form and are then combined to form an optimization model. The optimization is solved multiple times for different design parameters and requirements to observe changes in aircraft size and weight.

The driving requirement that sizes solar-electric powered aircraft is the ability to operate at multiple locations and during all seasons. To fly multiple days, solar-electric powered aircraft must carry enough solar cells and batteries to fly during the day while storing enough energy to fly through the night.[6] If this condition can be achieved during the winter solstice, when the solar flux is at a minimum, then a solar-electric powered aircraft can theoretically fly during any time of the year for long durations. [6] This becomes more difficult to achieve at higher latitudes as solar flux during the winter solstice decreases. Additionally, to station keep the aircraft must fly faster than the local wind speeds. Wind speeds are a function of latitude, altitude, and season and tend to increase at higher latitudes and during winter months. Therefore, a key sizing study of solar-electric powered aircraft is the effect of latitude on aircraft size.

The key driving requirement for a gas powered aircraft is endurance. As gas-powered aircraft are endurance limited by the amount of fuel that they can carry, longer endurance requires more fuel and hence a larger aircraft. Because gas-powered aircraft are not affected by the solar flux, their station-keeping ability at different latitudes only depends on the local wind speed. If a gas-powered aircraft can fly at the latitude with the worst wind speed, it can theoretically fly anywhere else in the world.

Using this geometric programming methodology, trade offs are observed between different aircraft configurations, power sources, and requirements. The results show that gas-powered aircraft can generally be built lighter and can fly faster and can therefore fly at higher latitudes and in higher percentile wind speeds. Solar-powered aircraft have greater endurance but are limited operationally by their ability to reach higher speeds. The presented optimization methodology can quantify the difference in weight and endurance between gas and solar-electric powered aircraft for the same set of requirements. Varying mission requirements reveals how the best architecture changes depending on the requirements.

II. Mission Requirements

A comparison of the gas and solar-electric powered aircraft is achieved by comparing their respective capabilities at satisfying a common set of requirements shown in Table 1. These requirements can and will be changed in the results section to observe which architecture is best suited to meet various sets of requirements. A discussion of each requirement is included in this section.

Table 1: Mission Requirements

Payload	10 lbs
Station Keeping	90% winds
Endurance	> 6 days
Season	all seasons
Altitude	> 4,600 m
Latitude	$\pm 30^\circ$

A. Station Keeping

To station keep an aircraft must fly at least as fast as the wind speed,

$$V \geq V_{\text{wind}}. \quad (1)$$

Distributions of wind speed data[7] indicate that it is impractical for long-endurance UAVs to station keep in 100 percentile wind speeds. Therefore, the station keeping requirement is parameterized by a percentile wind speed, p_{wind} , above which the aircraft is allowed to drift off station. The wind speed at a station is also a function of latitude, altitude, season or day of the year,

$$V_{\text{wind}} = f(\phi, h, \text{DOY}, p_{\text{wind}}). \quad (2)$$

Wind speed data was collected from the ERA Interim atmospheric datasets for the years 2005-2015.[7] It is assumed that the wind speed distribution is independent of longitude.

To meet the season requirement, the solar-electric aircraft must be able to fly a full day/night cycle on the winter solstice. If it can do so, it automatically exceeds the endurance requirement. To achieve this design constraint the aircraft must be able to fly with limited solar energy, discussed in Section V.B, and with higher than average wind speeds as shown in Figure 1.

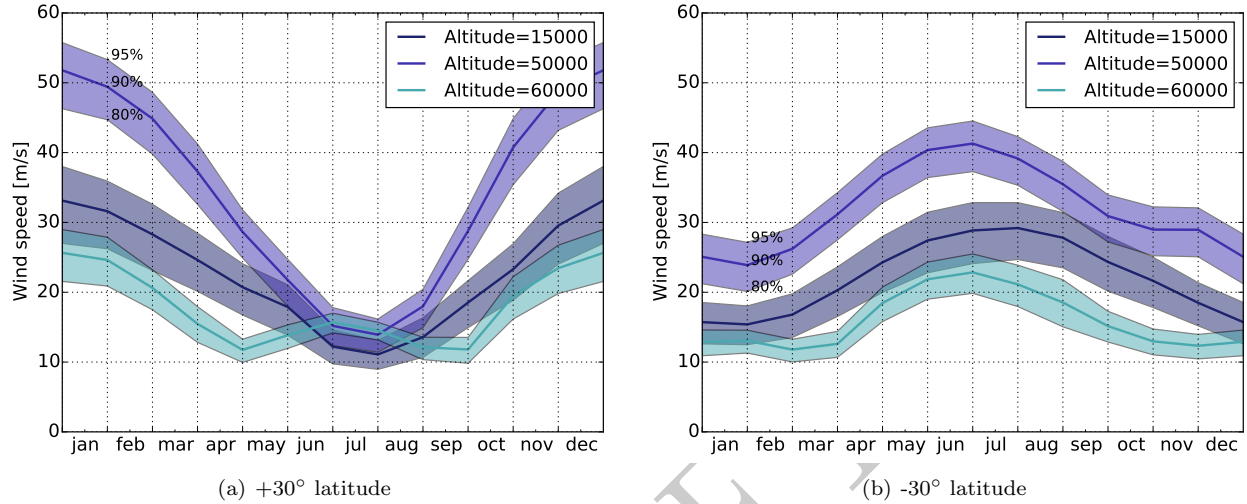


Figure 1: Winds peak at the winter solstice in Southern and Northern Hemispheres.[7]

For long-endurance gas powered aircraft, the endurance requirement is the amount of time the aircraft needs to remain in the air without refueling. This is expected to be mostly independent of season, except insofar as the wind speeds depends on season.

Because wind speeds are greatest during the winter solstice for both the Northern and Southern Hemispheres, only wind speeds from December and June, respectively, will be used for the both the gas and solar-electric powered aircraft sizing and performance analysis.

B. Altitude

One altitude requirement is a minimum height required to meet a certain coverage footprint,

$$h \geq h_{\min}. \quad (3)$$

Long-endurance aircraft tend to fly at low speeds, which based on Figure 2 means there are two possible operating altitude regimens: at or around the minimum height requirement of 4,600 m, or at high altitudes between 16,700-20,000 m. Gas powered aircraft generally fly in the lower altitude regime of 4,600 m because naturally aspirated engines lose power with increased altitude and are unable to reach altitudes higher than about 13,500 m. Solar-electric powered aircraft, which do not have naturally aspirated engines, will fly around 18,000 m to avoid cloud coverage.

C. Latitude

It is assumed that long-endurance aircraft will have a requirement to be capable of operating anywhere within a band of latitudes. For example, an aircraft designed or optimized for the 35th latitude would be able to operate at any latitude between ± 35 degrees. Latitude affects both the solar-electric and the gas powered aircraft because wind speed varies with latitude. Figure 3 shows how the wind speed varies with latitude in the Northern Hemisphere in December.

Latitude additionally affects the solar-electric powered aircraft because at higher latitudes there is less daylight and therefore less solar energy during the winter months. This is further discussed in Section V.B.

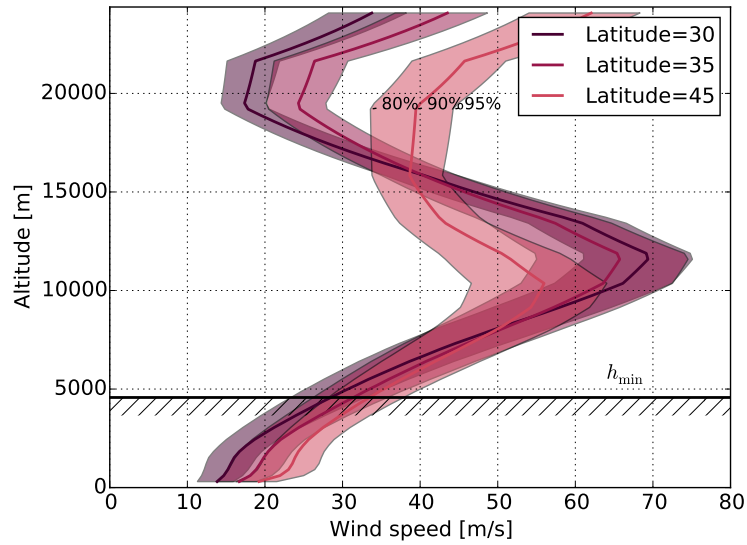


Figure 2: Aircraft must fly above h_{\min} to meet altitude requirement. Bands represent 80th, 90th and 95th percentiles.[7]

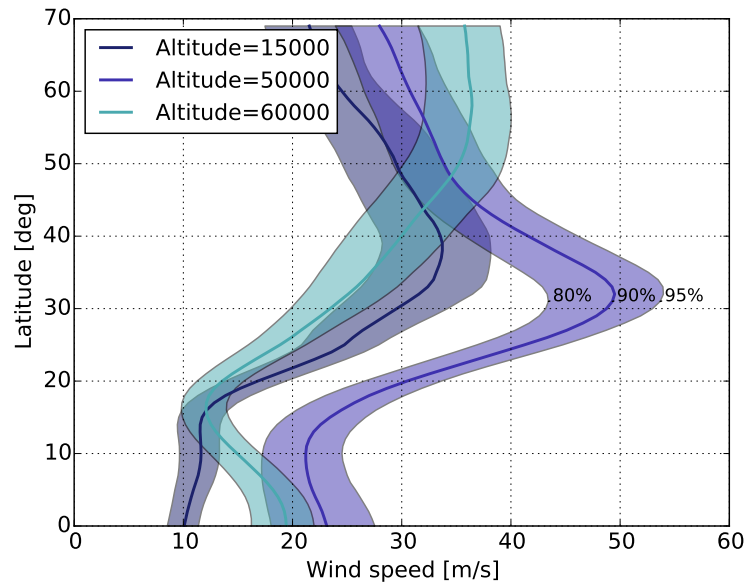


Figure 3: Wind speeds by latitude. Bands represent 80th, 90th and 95th percentile winds.[7]

III. Geometric Programming

Sizing long-endurance aircraft for the stated requirements was accomplished using geometric programming. Geometric programs (GPs) are a mathematical optimization problem characterized by the convexity of the objective and constraint functions.[5] GPs have the form

$$\begin{aligned}
& \text{minimize } f_0(\mathbf{x}) \\
& \text{subject to } f_i(\mathbf{x}) \leq 1, i = 1, \dots, m \\
& \quad \quad \quad g_i(\mathbf{x}) = 1, i = 1, \dots, p
\end{aligned} \tag{4}$$

where the functions g_i must be *monomial* functions and the functions f_i must be *posynomial* functions. *Monomials* and *posynomials* have the forms

$$g(\mathbf{x}) = cx_1^{a_1} x_2^{a_2} \dots x_n^{a_n}, \tag{6}$$

$$f(\mathbf{x}) = \sum_{k=1}^K c_k x_1^{a_{1k}} x_2^{a_{2k}} \dots x_n^{a_{nk}}. \tag{7}$$

The properties of a geometric program allow solution algorithms to guarantee convergence to a global optimum, provided that there exists a feasible solution to the set of constraint functions. Additionally, geometric programs can be solved rapidly with existing algorithms. Using state of the art, standard interior-point algorithms, GPs with 1,000 variables and 10,000 constraints converge to a solution in tens of seconds.[5]

To evaluate the gas and solar-electric powered design space, the requirements, architecture type, physical models, and assumed parameter values are expressed as constraints on the GP.[8] Essentially, the gas and solar-electric powered geometric programs are long lists of constraints in a GP-form that can be rapidly solved using interior point methods. Figure 4 shows how the optimization problem is constructed and solved. The following sections explain in detail the configuration, physical modeling, and input value assumptions and their resulting constraint equations that were used in both the gas and solar-electric powered optimization models.

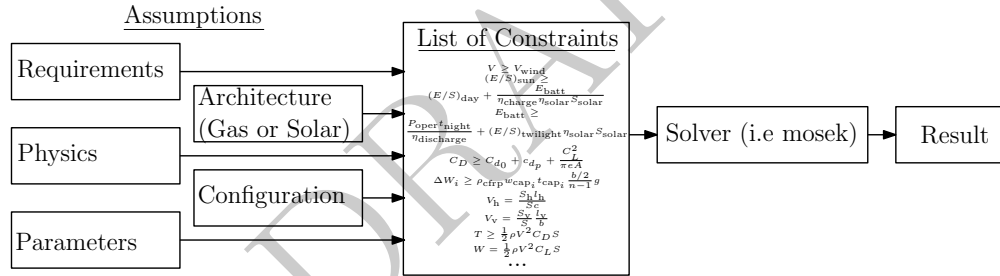


Figure 4: Process of constructing and solving a GP optimization problem.

A python package for defining and manipulating geometric programs, GPKit[9], is used to create the models described in this paper. A commercial solver, mosek[10], is used to solve the GP. Both the gas and solar-electric powered GP optimization models are available for download and use. [11]

IV. Configuration

For this study a simple fixed-wing tractor configuration was chosen as the baseline for both architectures. Common characteristics between the gas and solar models include a constant tapered wing and a conventional tail with a single tail boom extending from the wing. The gas powered aircraft has a fuselage to hold all of the fuel required for the mission. The solar-electric powered aircraft holds the batteries in the wings. The solar cells for the solar-electric aircraft are placed along the wing and possibly on the horizontal tail. A simple diagram of each vehicle is shown in Figure 5 with their corresponding weight breakdowns in Figure 6. The configuration is assumed to be static for this study.

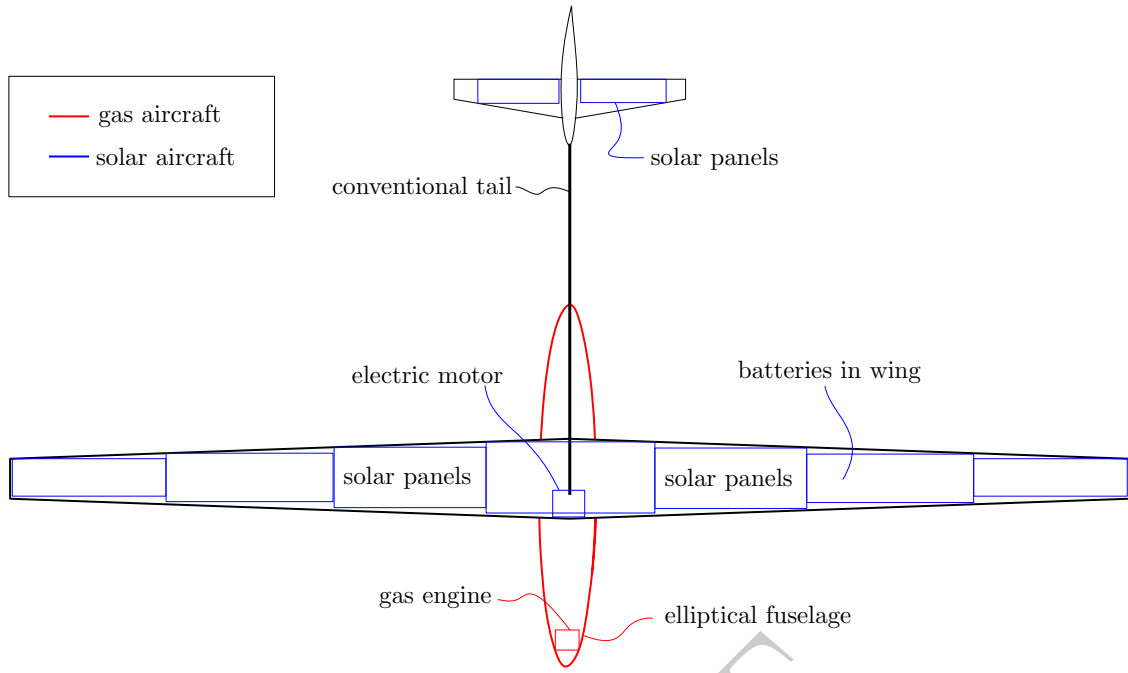


Figure 5: Blue and red are specific to the solar-electric and gas architectures respectively. Black are shared characteristics.

V. Aircraft Physical Models

To evaluate the size and performance of both gas and solar-electric powered aircraft, underlying physics models are used. Environmental, aircraft performance, and structural models are used in the optimization model to capture the effects of the requirements on the size and design of the aircraft. Equations from these models are expressed in a GP-compatible form to enable their use in the optimization. Understanding the models that are used in a GP is important because the solution to a GP is only as accurate as the models that are used to construct the program. To obtain higher fidelity results from the optimization, more detailed models can be implemented.

A. Shared Physical Models

The models described in this section were applied to both the gas powered and solar-electric powered aircraft models.

1. Steady Level Flight

Both the gas and solar powered aircraft are assumed to be in steady level flight,[8]

$$T \geq \frac{1}{2}\rho V^2 C_D S \quad (8)$$

$$W = \frac{1}{2}\rho V^2 C_L S. \quad (9)$$

The shaft power produced by the engine or motor can be expressed as

$$P_{\text{shaft}} = \frac{TV}{\eta_{\text{prop}}} \quad (10)$$

where the propulsive efficiency is assumed to be a constant, $\eta_{\text{prop}} = 0.8$.

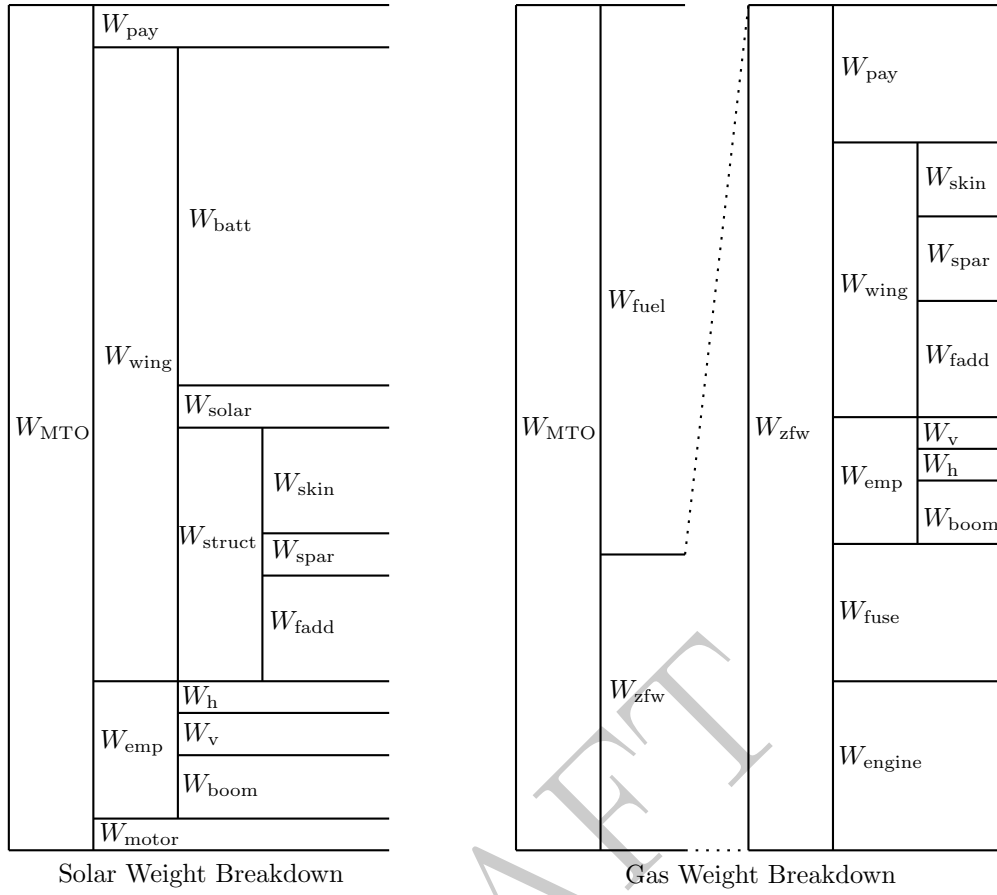


Figure 6: Representative weight breakdown of both aircraft optimization models.

2. Aerodynamics

The aircraft aerodynamics is modeled as a drag build up of the non-wing drag, wing profile drag, and induced drag coefficients,

$$C_D \geq C_{d_0} + c_{d_p} + \frac{C_L^2}{\pi e A}. \quad (11)$$

where the span efficiency factor is assumed to be constant, $e = 0.9$. The non-wing drag coefficient C_{d_0} , is estimated as a drag build up from the fuselage, tail boom, and horizontal and vertical surfaces discussed later.

To estimate the wing profile drag, a posynomial fit is made of the drag polar of the selected *JH01* airfoil (See Appendix A for a discussion of the airfoil choice). Drag polars were produced using XFOIL[23] at various Reynolds and the data was then fit to a posynomial equation. (See Appendix B) The XFOIL drag polar data is compared to the posynomial fit in Figure 7.

3. Wing Spar Model

A wing spar is one of the primary structural elements of both aircraft. A conservative approach to calculating the size of the spar is to assume that the spar carries all of the bending loads caused by the lifting loads and weight of the aircraft. It is assumed that there are two out of plane bending cases to which both the gas powered and the solar-electric powered aircraft are subject: standard wing bending and gust loads.

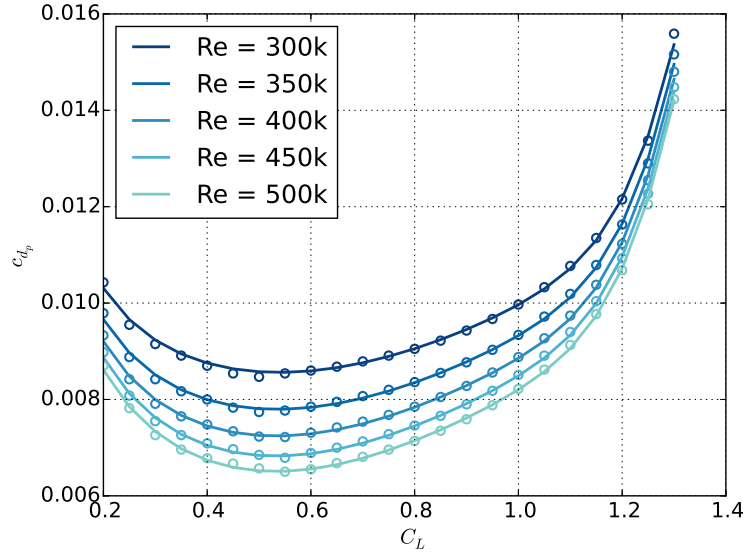


Figure 7: Posynomial fit (solid lines) to XFOIL data (circles). (Log-space RMS error = 0.00489.)

Standard Wing Bending Case The distributed load along the wing is a combination of the lifting and weight distributions along the wing. The wing loading distribution $q(y)$, can be approximated as a scaling of the local chord,[24]

$$q(y) \approx K_q c(y) \quad (12)$$

where y is the distance from the root wing location. The loading constant K_q [24], is defined as

$$K_q = \frac{N_{\max} W_{\text{cent}}}{S} \quad (13)$$

where W_{cent} is the sum of loads acting at the center of the aircraft and the safety load factor is an input $N_{\max} = 5$ ($N_{\max} = 1$ corresponds to steady level flight). Using the equation for the local chord of a constant tapered wing[24] with a taper ratio $\lambda = 0.5$, the pre-computed distributed load

$$\bar{q}(y) \equiv \frac{q(y)b}{N_{\max} W_{\text{cent}}} = \frac{2}{1 + \lambda} \left(1 + (\lambda - 1) \frac{2y}{b} \right), \quad (14)$$

is inputted into a standard beam model to predict the bending moments and deflections. The center weight W_{cent} for the gas powered aircraft is

$$W_{\text{cent}} \geq W_{\text{fuel}} + W_{\text{fuselage}} + W_{\text{engine}} + W_{\text{payload}} + W_{\text{emp}}. \quad (15)$$

The center weight for the solar powered aircraft is

$$W_{\text{cent}} \geq W_{\text{payload}} + W_{\text{motor}} + W_{\text{emp}}. \quad (16)$$

Gust Loading Case Because long-endurance aircraft typically have high aspect ratio wings, they are considered flexible aircraft. To account for this flexibility and size a structural wing spar that will ensure enough rigidity in the event of a gust load, a distributed gust lifting load is added to the steady level flight loading distribution

$$q(y) = \frac{N_{\max} W_{\text{cent}}}{b} \bar{c}(y) + c_{l_\alpha} \alpha_{\text{gust}} \frac{1}{2} \rho V^2 \frac{S}{b} \bar{c}(y) \quad (17)$$

$$\bar{q}(y) = \frac{q(y)b}{W_{\text{cent}} N_{\max}} \geq \bar{c}(y) \left[1 + \frac{c_{l_\alpha}}{C_L} \alpha_{\text{gust}}(y) \left(1 + \frac{W_{\text{wing}}}{W_{\text{cent}}} \right) \right] \quad (18)$$

where $\bar{c}(y)$ is pre-computed prior to the optimization solve for a taper ratio $\lambda = 0.5$. The safety load factor is $N_{\max} = 2$ for the gust loading case. The weight of the wing for the gas powered aircraft is assumed to be the weight of the spar cap plus the weight of the skin

$$W_{\text{wing}} \geq W_{\text{spar}} + W_{\text{skin}}. \quad (19)$$

For the solar-electric powered aircraft the batteries and solar cells are also included in the wing weight

$$W_{\text{wing}} \geq W_{\text{spar}} + W_{\text{skin}} + W_{\text{batt}} + W_{\text{solar}}. \quad (20)$$

The gust velocity is assumed to be vertical to the flight path such that the local angle of attack is approximated by

$$\alpha_{\text{gust}}(y) = \tan^{-1} \left(\frac{V_{\text{gust}}(y)}{V} \right). \quad (21)$$

Because the arctan function is not GP compatible, a monomial approximation was calculated using techniques described by Hoburg et. al[12],

$$\alpha_{\text{gust}}(y) = 0.946 \left(\frac{V_{\text{gust}}(y)}{V} \right)^{0.996} \quad (22)$$

and has an RMS log-space error of 0.039 for $V_{\text{gust}}/V \in [0, 0.7]$. The gust velocity has an assumed profile along the wing[25],

$$V_{\text{gust}}(y) = V_{\text{ref}} \left(1 - \cos \left(\frac{2y}{b} \frac{\pi}{2} \right) \right) \quad (23)$$

where the reference velocity is an assumed conservative value[25], $V_{\text{ref}} = 10$ [m/s]. The gust velocity profile is computed prior to solve to preserve GP-compatibility.

Discretized Beam Model Using a standard Bernoulli-Euler discretized beam model with $n = 5$ nodes[24], the shear forces, moments, angles, and deflections can be expressed in a GP-compatible form using the distributed loads $q(y)$, as an input,

$$\mathcal{S}_{i+1} \geq \mathcal{S}_i + \frac{q_{i+1} + q_i}{2} \Delta y \quad (24)$$

$$\mathcal{M}_{i+1} \geq \mathcal{M}_i + \frac{\mathcal{S}_{i+1} + \mathcal{S}_i}{2} \Delta y \quad (25)$$

$$\Theta_i \geq \Theta_{i+1} + \frac{1}{2} \left(\frac{\mathcal{M}_i}{EI_i} + \frac{\mathcal{M}_{i-1}}{EI_{i-1}} \right) \Delta y \quad (26)$$

$$w_i \geq w_{i+1} + \frac{1}{2} (\Theta_i + \Theta_{i-1}) \Delta y. \quad (27)$$

where the Young's Modulus of carbon fiber is $E = 20$ [MPa]. Boundary conditions are zero shear forces and moments at the wing tips and zero angle and deflection at the wing root.[24]

Cap Spar for Bending Loads A cap spar is considered for the solar-electric and gas powered aircraft. A cap spar has two carbon fiber caps separated by a foam core as seen in Figure 8. A thin shear web is wrapped around the caps and foam to prevent shearing and buckling.

The moment of inertia of the cap spar is modeled by only considering the spar caps, not the foam interior. This conservative assumption is made because the contribution of the foam core is much less than that of the spar caps. The equation for the moment of inertia[24] of a cap spar is

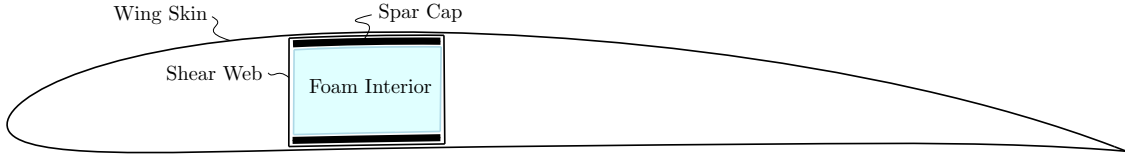


Figure 8: Cross sectional view of a cap spar.

$$I = \frac{w_{\text{cap}} t_{\text{cap}}^3}{6} + 2w_{\text{cap}} t_{\text{cap}} \left(\frac{h_{\text{cap}}}{2} + \frac{t_{\text{cap}}}{2} \right)^2. \quad (28)$$

This equation is not GP compatible. However, using a first order conservative approximation, the moment of inertia can be simplified to be written in a GP-compatible form,

$$I \leq 2w_{\text{cap}} t_{\text{cap}} \left(\frac{h_{\text{cap}}}{2} \right)^2. \quad (29)$$

There are also geometric constraints imposed on the width and thickness. The total spar cap thickness cannot be greater than the thickness of the airfoil cross section, $\tau_t = 0.115$. The width of the spar cap is assumed no greater than 30% of chord, $\tau_w = 0.3$.

$$c(y)\tau_t \geq h_{\text{cap}} + 2t_{\text{cap}} \quad (30)$$

$$c(y)\tau_w \geq w_{\text{cap}} \quad (31)$$

To match the discretized beam model, the spar cross section can also be written in a discretized form such that each section has a unique width and thickness.

$$I_i \leq 2w_{\text{cap}_i} t_{\text{cap}_i} \left(\frac{h_{\text{cap}_i}}{2} \right)^2 \quad (32)$$

$$c(y)\tau_t \geq h_{\text{cap}_i} + 2t_{\text{cap}_i} \quad (33)$$

$$c(y)\tau_w \geq w_{\text{cap}_i} \quad (34)$$

The wing spar at each section root must be strong enough to withstand the bending moment and stiff enough to not exceed some deflection limit. Both constraints are imposed in the optimization model as

$$\sigma_{\text{cfrp}} \geq \mathcal{M}_i \frac{h_{\text{cap}_i} + t_{\text{cap}_i}}{I_i} \quad (35)$$

$$w_n \leq w_{\text{max}} \quad (36)$$

where the ultimate tensile strength for unidirectional carbon fiber is $\sigma_{\text{cfrp}} = 1700$ [MPa].[26] The tip deflection is constrained to be less than 20% of the half span, $\frac{w_{\text{max}}}{b/2} = 0.2$.

Finally, the weight of the spar cap is computed as

$$\Delta W_i \geq \rho_{\text{cfrp}} w_{\text{cap}_i} t_{\text{cap}_i} \frac{b/2}{n-1} g \quad (37)$$

$$W_{\text{spar}} \geq 2 \sum_{i=1}^{n-1} \Delta W_i \quad (38)$$

where $\rho_{\text{cfrp}} = 1.6$ [g/cm³].[16]

4. Additional Wing Weight

It is assumed that the wing skin is made of carbon fiber. The weight of the wing skin is

$$W_{\text{skin}} \geq 2\rho_{A_{\text{cfRP}}} Sg. \quad (39)$$

where $\rho_{A_{\text{cfRP}}} = 0.049$ [g/cm²], or approximately the area density of one ply of carbon fiber.[16] The wing skin is assumed not to contribute to the bending stiffness.

Additional wing weight W_{fadd} , accounts for additional structural weight (ribs, rear spar, actuators, etc.),

$$W_{\text{fadd}} \geq (W_{\text{spar}} + W_{\text{skin}})m_{\text{fac}} \quad (40)$$

where $m_{\text{fac}} = 1.2$.

5. Empennage

An empennage model is added to both the solar-electric and gas powered aircraft models. The empennage model consists of a single tail boom, horizontal tail and vertical tail. The empennage adds both weight and drag to each aircraft.

The tail boom has an optimized diameter d , root wall thickness t_0 , root moment of inertia I_0 , modulus $E = 150$ [GPa][26], density $\rho_{\text{cfRP}} = 1.6$ [g/cm³][26], and length l_h . The total mass and root bending inertia are imposed in the optimization model as

$$m \geq \pi\rho_{\text{cfRP}}t_0dl_h \left(1 - \frac{1}{2}k\right) \quad (41)$$

$$I_0 \leq \pi t_0 d^3 / 8 \quad (42)$$

where the index $k = 0$ corresponds to a uniform wall thickness and stiffness, and $k = 1$ corresponds to a linear drop-off to zero. For both the solar-electric and gas powered aircraft $k = 0.8$ is assumed. When the tail boom is loaded at the endpoint $x = l_h$, by the horizontal tail lift L_h , the end deflection angle follows from standard beam analysis

$$\theta \geq \frac{L_h l_h^2}{EI_0} \frac{1+k}{2} \quad (43)$$

$$L_h = \frac{1}{2}C_{L_h}\rho V^2 S_h. \quad (44)$$

The horizontal tail is sized to satisfy a horizontal tail volume coefficient condition $V_h = 0.45$,[27]

$$V_h = \frac{S_h l_h}{S_c} \quad (45)$$

The vertical tail is sized to meet a conservative tail volume coefficient $V_v = 0.04$,[27]

$$V_v = \frac{S_v l_v}{S b} \quad (46)$$

where l_v is the vertical tail moment arm, assumed to be equal to the horizontal tail moment arm, $l_v = l_h$.

Both the horizontal and vertical tails are assumed to have a carbon fiber skin and solid foam interior where their respective densities are $\rho_{A_{\text{cfRP}}} = 0.049$ [g/cm²], $\rho_{\text{foam}} = 1.5$ [lb/ft³]. The weight of the tails is

$$W_{(v,h)}/m_{\text{fac}} = \rho_{\text{foam}} \frac{S_{(v,h)}^2}{b_{(v,h)}} \bar{A} + g\rho_{A_{\text{cfRP}}} S_{(v,h)} \quad (47)$$

where b_h and b_v are the spans of the horizontal and vertical tails respectively and \bar{A} is the cross sectional area of the NACA 0008 airfoil. The margin factor $m_{\text{fac}} = 1.1$, is included to account for control surfaces, attachment joints, actuators, etc.

The drag of the empennage was modeled as three separate parts with no interference drag. The drag of the tail boom is calculated using a turbulent flat plate model,

$$D_{\text{boom}} \geq \frac{1}{2} C_f \rho V^2 l_h \pi d \quad (48)$$

$$C_f \geq \frac{0.445}{Re_{\text{boom}}^{0.3}} \quad (49)$$

$$Re_{\text{boom}} = \frac{V \rho l_h}{\mu} \quad (50)$$

The drag of the horizontal and vertical tails is computed using a GP-compatible fit of XFOIL data for a range of Reynolds numbers and NACA airfoil thicknesses, where the selected airfoil is the NACA 0008 for both the horizontal and vertical tails (i.e. $\tau_{(v,h)} = 0.08$). The XFOIL data was generated for a zero angle of attack, based upon steady level flight where neither surface is generating lift.

B. Solar-Electric Aircraft Physical Models

1. Wind Speeds

There exists an optimum flight altitude for solar-electric powered aircraft. The local minimum in wind speed around 19,000 m and the variation of air density with altitude suggest that the altitude should be an output of the optimization. To accomplish this, constraints relating wind speed to altitude are imposed. This approach assumes that the solar-electric powered aircraft will not be confined to fly at a single altitude, but will fly at the altitude where conditions are most favorable.

Because wind speeds do not increase monotonically with latitude, it is possible that the design for a given latitude is constrained by winds at a latitude inside the required latitude band. To handle this, a multipoint set of latitude constraints is imposed. The wind speed data used to generate these equations includes December wind speeds from the Northern Hemisphere and June wind speeds from the Southern Hemisphere for the years 2005-2015. In total, 41 wind speed constraints were generated to represent ± 20 -60 degrees each with a log space RMS error of less than 5%. (See Appendix B)

For the gas powered aircraft, the altitude is not optimized. Gas-powered aircraft, which are naturally aspirated, will be less efficient at higher altitudes. Additionally, wind speeds increase monotonically from sea level up to $\sim 9,100$ m. Therefore, the altitude for gas-powered aircraft is determined as the minimum altitude necessary for the payload to be effective.[3] For this sizing study, the altitude requirement for the gas powered aircraft is $h_{\text{min}} = 4,500$ m, corresponding to a 100 km diameter footprint with a 5 degree lookup angle.

2. Solar-Electric Power

At a given time of year DOY, and latitude ϕ , there exists an available solar irradiated energy $(E/S)_{\text{sun}}$ per unit area during one day,

$$(E/S)_{\text{sun}} = f(\phi, \text{DOY}). \quad (51)$$

To operate continually for multiple days the total available solar energy $(E/S)_{\text{sun}}$, must be greater than the required pre-conversion-efficiency solar energy per unit area to power the aircraft during the day $(E/S)_{\text{day}}$, and the energy required to power the aircraft during the night via batteries E_{batt} ,[6]

$$(E/S)_{\text{sun}} \geq (E/S)_{\text{day}} + \frac{E_{\text{batt}}}{\eta_{\text{charge}} \eta_{\text{solar}} S_{\text{solar}}} \quad (52)$$

$$E_{\text{batt}} \eta_{\text{discharge}} \geq P_{\text{oper}} t_{\text{night}} + (E/S)_{\text{twilight}} \eta_{\text{solar}} S_{\text{solar}} \quad (53)$$

where the charge, discharge and solar cell efficiencies are assumed to be $\eta_{\text{charge}} = \eta_{\text{discharge}} = 0.98$ and $\eta_{\text{solar}} = 0.22$. An additional energy term $(E/S)_{\text{twilight}}$ is included in Equation (53) to account for hours of low solar irradiance, during mornings and evenings, when the aircraft must continue to fly on partial battery power. Equations (52) and (53) are graphically represented in Figure 9, which represents the solar energy at 30 degrees latitude.

In order for the aircraft to begin charging batteries there must be a minimum solar irradiance power

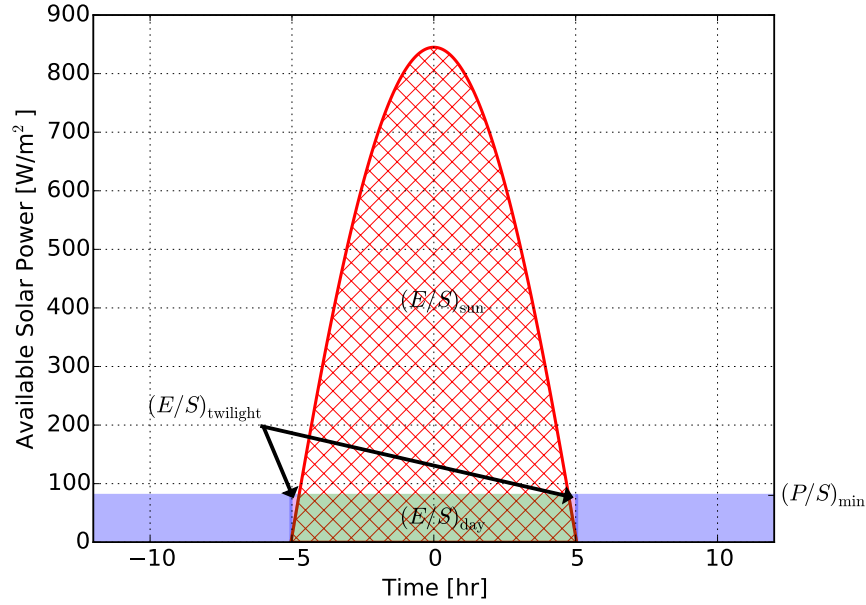


Figure 9: Solar power on Dec 21st at 30° North. 24-hour operationality achieved when red area exceeds blue, magenta and green areas.

$$(P/S)_{\min} = \frac{P_{\text{oper}}}{\eta_{\text{solar}} S_{\text{solar}}} \quad (54)$$

$$\eta_{\text{motor}} P_{\text{oper}} \geq P_{\text{shaft}} + P_{\text{avionics}}. \quad (55)$$

where $\eta_{\text{motor}} = 0.95$. Thus, for a given latitude and day, and therefore total solar energy $(E/S)_{\text{sun}}$, both $(E/S)_{\text{day}}$ and $(E/S)_{\text{twilight}}$ are functions of $(P/S)_{\min}$. The total solar energy available $(E/S)_{\text{sun}}$, is computed prior to the optimization solve and is used to generate monomial approximations for $(E/S)_{\text{day}}$ and $(E/S)_{\text{twilight}}$ as functions $(P/S)_{\min}$, one for each degree of latitude between 20 and 60 degrees latitude. $(E/S)_{\text{sun}}$, $(E/S)_{\text{day}}$, $(E/S)_{\text{twilight}}$, and t_{night} are precomputed using the formulas in Appendix C to generate the fitted equations.

For the purposes of this design study, it is assumed that the solar cells are placed on the wing and the horizontal tail but not on the vertical tail. The fractional solar cell area index f_{solar} is one when the solar cells completely cover the main wing and greater than one if solar cells are also placed on the horizontal tail,

$$S_{\text{solar}} \leq f_{\text{solar}} S. \quad (56)$$

3. Motor Weight

The solar-electric powered aircraft has a motor whose weight is based on the approximation[18]

$$P_{\text{max}} = B_{\text{PM}} m_{\text{motor}} \quad (57)$$

where m_{motor} is the motor mass, $P_{\text{max}} \geq P_{\text{oper}}$ is the maximum operating power, and the assumed power to mass ratio is $B_{\text{PM}} = 4140.8 \text{ [W/kg]}$.

C. Gas Powered Aircraft Physical Models

1. Breguet Endurance

A key sizing equation for a long endurance gas powered aircraft is the Breguet Range equation. For GP-compatibility and to optimize endurance, not range, a variation of the Breguet Range equation is used,

$$t = \frac{W_{\text{ave}}}{P_{\text{shaft}} \text{BSFC} g} \ln \left(\frac{W_{\text{initial}}}{W_{\text{final}}} \right). \quad (58)$$

This version comes from assuming that BSFC and the power to weight ratio, (P_{shaft}/W) , are constant during the considered flight segment. One way to obtain a constant power to weight ratio is a constant velocity and constant lift coefficient.[14] The segment weight, W_{ave} , is assumed to be the geometric mean, defined as

$$W_{\text{ave}} = \sqrt{W_{\text{initial}} W_{\text{final}}}. \quad (59)$$

To make Equation (58) GP compatible, a Taylor expansion is used,[8]

$$z_{\text{bre}} \geq \frac{P_{\text{shaft}} t \text{BSFC} g}{W} \quad (60)$$

$$\frac{W_{\text{fuel}}}{W_{\text{final}}} \geq z_{\text{bre}} + \frac{z_{\text{bre}}^2}{2} + \frac{z_{\text{bre}}^3}{6} + \frac{z_{\text{bre}}^4}{24} + \dots \quad (61)$$

Equations (60) and (61) are monomial and posynomial respectively and therefore GP compatible. For long-endurance aircraft, missions can last days, causing the power to weight ratio (P_{shaft}/W) to vary significantly during the course of the flight. Equations (60), (61), and (9) can be discretized to account for this,

$$\sqrt{W_i W_{i+1}} = \frac{1}{2} \rho_i V_i^2 C_{L_i} S \quad (62)$$

$$z_{\text{bre}_i} \geq \frac{P_{\text{shaft}_i} t_i \text{BSFC} g}{\sqrt{W_i W_{i+1}}} \quad (63)$$

$$\frac{W_{\text{fuel}_i}}{W_{i+1}} \geq z_{\text{bre}_i} + \frac{z_{\text{bre}_i}^2}{2} + \frac{z_{\text{bre}_i}^3}{6} + \frac{z_{\text{bre}_i}^4}{24}. \quad (64)$$

For evaluation of long-endurance, gas-powered aircraft a discretization of $N = 5$ was used.

2. Elliptical Fuselage

For the gas powered aircraft it is assumed that the fuel is carried in an elliptically shaped fuselage. The fuselage will increase the overall weight and drag of the aircraft. The solar-electric powered aircraft is assumed to carry the batteries in the wings will therefore have a small fuselage whose effects will be ignored.

The driving constraint for the size of the fuselage is to ensure that all of the fuel required for the mission can fit inside the fuselage,

$$\mathcal{V}_{\text{fuse}} \geq \frac{W_{\text{fuel}}}{\rho_{\text{fuel}}} \quad (65)$$

where the fuel is assumed to have a density $\rho_{\text{fuel}} = 6.01$ [lbf/gallon]. The dimensions of the fuselage are constrained by

$$\mathcal{V}_{\text{fuse}} \leq \frac{4}{3} \pi \frac{l_{\text{fuse}}}{2} R_{\text{fuse}}^2 \quad (66)$$

where l_{fuse} is the length of the fuselage and R_{fuse} is the radius. Using the length and radius, the surface area can be calculated using Thomsen's approximation,[15]

$$3 \left(\frac{S_{\text{fuse}}}{\pi} \right)^{1.6075} \geq 2(2l_{\text{fuse}} R_{\text{fuse}})^{1.6075} + (4R_{\text{fuse}}^2)^{1.6075}. \quad (67)$$

The weight of the fuselage is constrained by

$$W_{\text{fuse}} \geq S_{\text{fuse}} \rho_{A_{\text{cfRP}}} g \quad (68)$$

where $\rho_{A_{\text{cfRP}}} = 0.0975 \text{ [g/cm}^2\text{]}$, or the area density of two plies of carbon fiber.[16] The surface area is also used to calculate the drag assuming a skin friction based drag model,

$$D_{\text{fuse}} \geq C_f k_{\text{fuse}} \frac{1}{2} \rho V^2 S_{\text{fuse}} \quad (69)$$

$$C_f \geq \frac{0.455}{Re^{0.3}} \quad (70)$$

where k_{fuse} is the form factor approximated by[17]

$$k_{\text{fuse}} \geq 1 + \frac{60}{(l_{\text{fuse}}/2R_{\text{fuse}})^3} + \frac{(l_{\text{fuse}}/2R_{\text{fuse}})}{400}. \quad (71)$$

3. Engine Weight

The engine weight of the gas powered aircraft is governed by a simple power law derived from existing two-stroke and four-stroke engines[19]

$$\frac{W_{\text{engine}}}{W_{\text{engine-ref}}} = 1.27847 \left(\frac{P_{\text{SL-max}}}{P_{\text{ref}}} \right)^{0.772392} \quad (72)$$

where $W_{\text{engine-ref}} = 10 \text{ [lbs]}$ and $P_{\text{ref}} = 10 \text{ [hp]}$. Equation (72) is compared to the data in Figure 10.

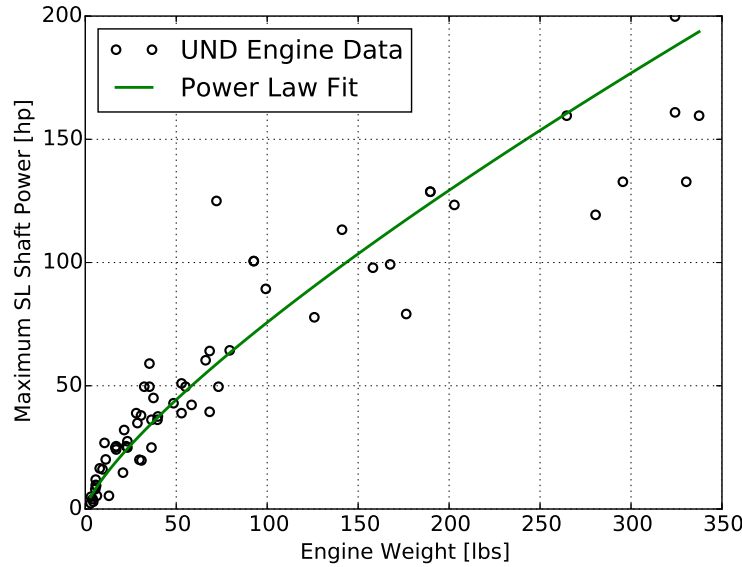


Figure 10: Power law fit to University of North Dakota engine weight data[19]. (Log-space RMS error = 0.34)

4. Gas Powered Engine Performance

Two characteristics of gas engines affect the performance of long-endurance aircraft. The first is brake specific fuel consumption, BSFC; a lower BSFC will result in increased endurance. The second is the lapse rate. Assuming a propeller driven aircraft and a naturally aspirated engine, as the aircraft reaches higher altitudes, the engine will have decreased available power. To account for these two effects a two-stroke, double cylinder engine, the DF70 from RCV Engines Ltd, England, was selected as a representative engine. RCV

Engines Ltd provided manufacturing data that was used to generate representative performance curves.[20] It is assumed that engines of a similar size will perform similarly to the DF70 engine. This engine performance model is only valid for internal combustion engines.

To capture throttling effects as aircraft weight decreases, a GP-compatible curve was generated from the DF70 data to relate BSFC and shaft power. (Figure 11) Using this approximation the required shaft power determines the BSFC. A comparison of the DF70 data provided by RCV Engine Ltd in Figure 11 to the BSFC to power curves in Goering[21] verify that this performance curve is representative of engines of similar sizes.

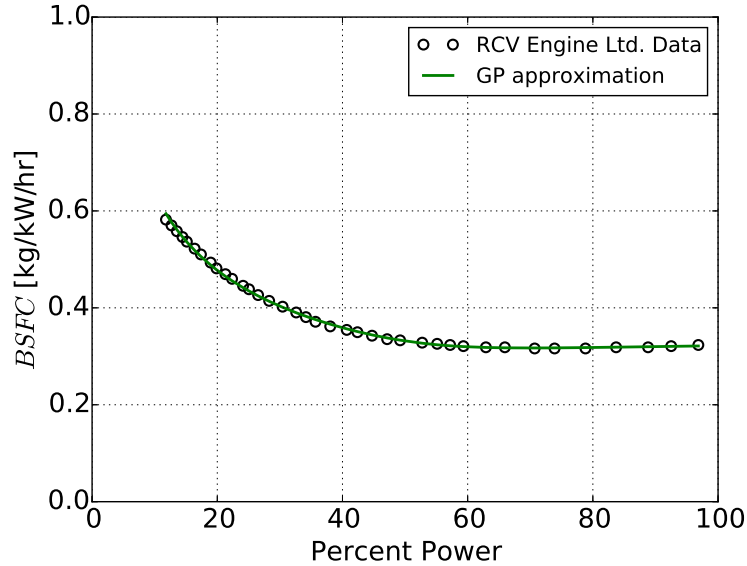


Figure 11: Representative engine performance fit based on RCV Engine Ltd data. (Log-space RMS error = 0.007)

The lapse rate $L_{\text{eng}}(h) \leq 1$, is assumed to affect the maximum power output,

$$L_{\text{eng}}(h) \equiv \frac{P_{\text{max}}}{P_{\text{SL-max}}}. \quad (73)$$

The lapse is calculated from the required flight altitude $h = 4,500$ [m], prior to the optimization solve using an approximate engine loss rate for normally aspirated engines of 3.5% hp per 300 m,[22]

$$L_{\text{eng}}(h) = 1 - \frac{0.035}{300 \text{ [m]}} h. \quad (74)$$

5. Climb Constraints

Because the gas engine is naturally aspirated, as the aircraft climbs there will be less available power. The climb constraint ultimately sizes the engine because at the top of climb, when the least amount of power is available, the engine must provide the necessary power to meet a minimum climb rate,

$$\dot{h}_{\text{min}} \geq 30 \text{ [m/min]}. \quad (75)$$

The climb rate affects the required thrust, and therefore the required power during climb,

$$T \geq \frac{1}{2} C_D \rho V^2 S + W \frac{\dot{h}_{\text{min}}}{V} \quad (76)$$

where W is the weight of the aircraft during climb.

VI. Results

The gas and solar-electric powered aircraft optimization models were solved by minimizing the take-off weight for the requirements listed in Table 1. Key design parameters for both aircraft optimization models are listed in Table 2. The gas powered aircraft optimization model had 552 unknowns and was solved in 0.144 seconds for a max take-off weight of 84.0 lbs. The solar-electric powered optimization model had 375 unknowns and was solved in 0.164 seconds for a max take-off weight of 320.5 lbs. According to the assumptions described in the previous section, the gas powered aircraft is better suited to meet this specific set of requirements. This section explores how this result may vary for different requirements, input parameter values, and physics modeling assumptions.

Table 2: Fixed Optimization Parameters

Gas Powered		Solar Powered	
η_{prop}	0.8	η_{prop}	0.8
τ	0.115	τ	0.115
λ	0.5	λ	0.5
σ_{CFRP} [MPa]	1700	σ_{CFRP} [MPa]	1700
N_{max} - g-Loading	5	N_{max} - g-Loading	5
N_{max} - gust load	2	N_{max} - gust load	2
BSFC _{100%} [kg/hr/kW]	0.31	η_{solar}	0.22
Lapse Rate [hp/1000 ft]	0.035	h_{batt} [Whr/kg]	350
\dot{h}_{min} [ft/min]	100	η_{motor}	0.95
ρ_{fuel} [lbf/gallon]	6.01	η_{charge}	0.98
		$\eta_{\text{discharge}}$	0.98

A. Changing Requirements

Important trade offs between the gas powered and solar-electric powered architectures are highlighted and quantified by changing the latitude and endurance requirements. Both optimization models were solved by minimizing the max take-off weight across different latitude requirements. Figure 12 shows this result evaluated at the 80th, 90th and 95th percentile wind speeds. The gas powered model was solved 63 times in 5.6178 seconds total and the solar-electric powered model was solved 31 times in 2.5529 seconds total to produce Figure 12.

One way to interpret Figure 12 is that a solar-powered aircraft weighing 190 lbs is able to operate between ± 28 degrees latitude in 90th percentile wind speeds. This analysis shows that gas powered architectures are able to operate in more locations than solar-electric powered aircraft. On the other hand, solar-electric powered aircraft design becomes infeasible at higher latitudes because even though wind speeds peak around 42 degrees latitude at 18,300 m, the combination of lower solar flux and higher wind speeds makes it difficult to reach latitude bands greater than ± 30 degrees.

While the solar-electric powered aircraft may be limited operationally by higher latitudes, it is not limited in endurance as is the gas powered aircraft. Solving the gas powered optimization model for different endurance requirements shows where the gas powered architecture becomes less feasible. Figure 13 shows the endurance versus size analysis for a gas powered aircraft by minimizing max take-off weight for an aircraft capable of flying at any latitude. Figure 13 was generated using 29 separate optimization solutions that took a total of 2.403 seconds to solve.

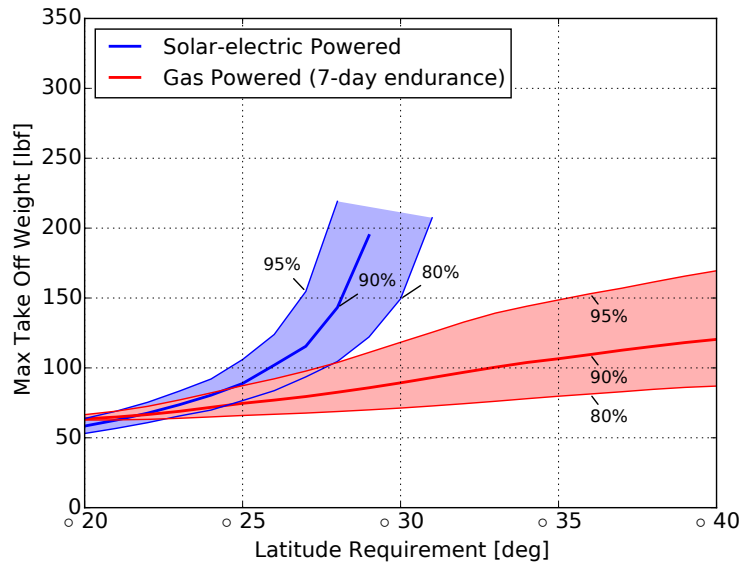


Figure 12: Gas architecture feasible for all latitudes. Next integer latitude for each solar-electric curve is infeasible.

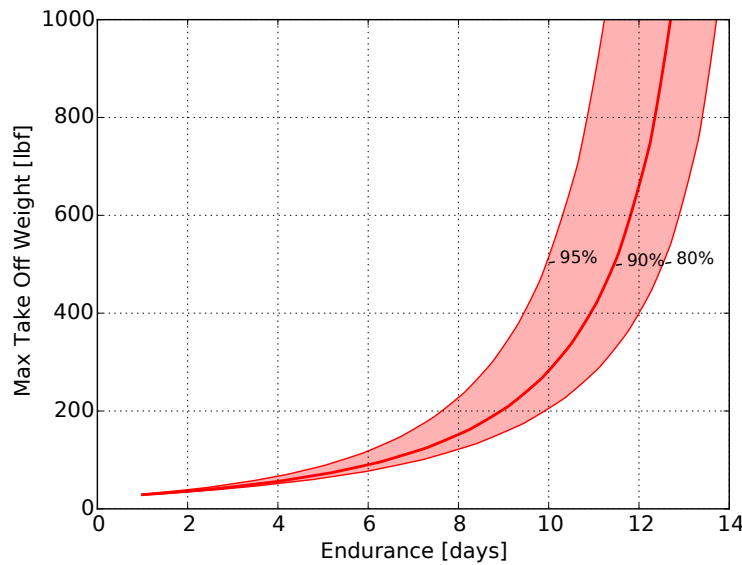


Figure 13: Endurance and size trade study for gas powered architecture.

B. Changing Parameter Values

The previous results are dependent on the assumed input values and parameters. Changing parameter values can help show where the designs become infeasible. As one example, two input values that are especially important to the solar aircraft are the solar cell efficiency and battery specific energy. By solving the model for different assumed solar cell efficiency and battery specific energy values a broader picture of the design space is achieved. Figure 14 shows contours of latitude for a given solar cell efficiency and battery energy density. Put another way, this plot shows how good the solar cells and batteries must be in order to reach a given latitude. Figure 14 was produced using 157 separate optimization solutions that took a total of 14.379 seconds to solve.

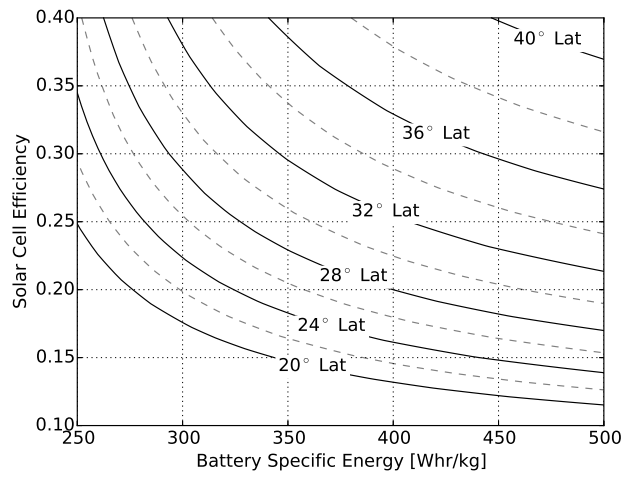


Figure 14: Contours of latitude. Reaching higher latitudes requires better solar cells and batteries.

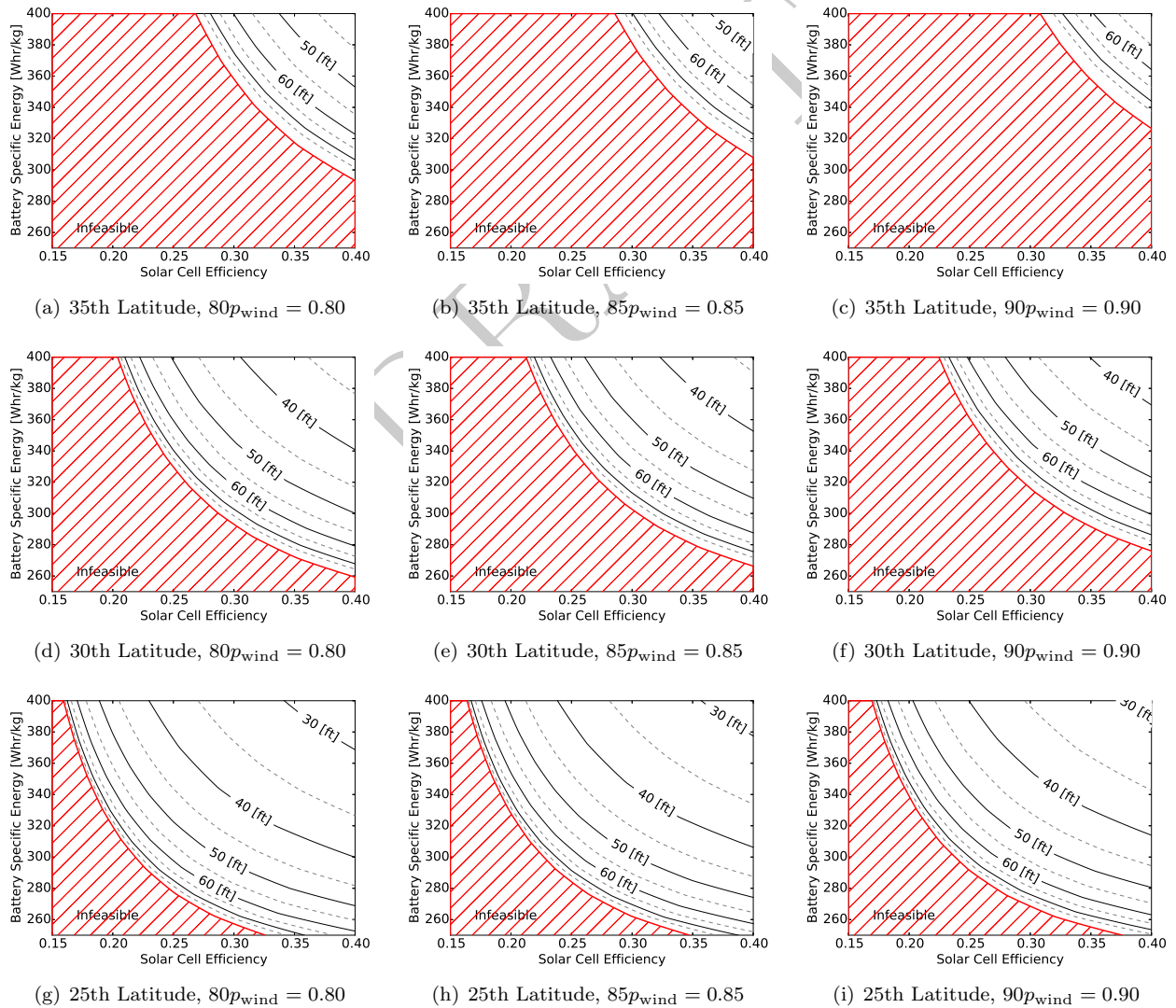


Figure 15: Matrix of minimum wing span solar-electric aircraft designs. Values of assumed constants are given throughout the text.

Figure 15 shows a matrix contour map of the solar-electric powered aircraft wing spans for multiple solar cell efficiencies, battery energy densities, latitudes, and percentile wind speeds. Each point in Figure 15 is a unique design for minimum wing span. The infeasible regions and contour shapes would change for different assumed constant values.

C. Changing Physical Modeling Assumptions

Insight into the design space can also be gained by changing the physical modeling assumptions. For example, by altering the aircraft structural model it can be observed how air density trades for wing weight. It might be assumed that because the wind speeds are lowest at 20,400 m at 29 degrees latitude, that the aircraft will always fly at 20,400 m. If it is assumed that the structural weight of the aircraft can be modeled as a fraction of the total weight

$$W_{\text{structural}} \geq W_{\text{MTO}} f_{\text{structural}} \quad (77)$$

where $f_{\text{structural}} = 0.35$, then the optimized flight altitude is almost exactly 67,000 ft as shown in Figure 16. However, if the structural weight is represented by the more detailed model as explained in Section V, larger wings have a weight penalty and the optimization trades air density for wing weight. Therefore, by adding a structural model the optimization seeks a smaller wing to save weight and operates at a lower altitude to increase density.

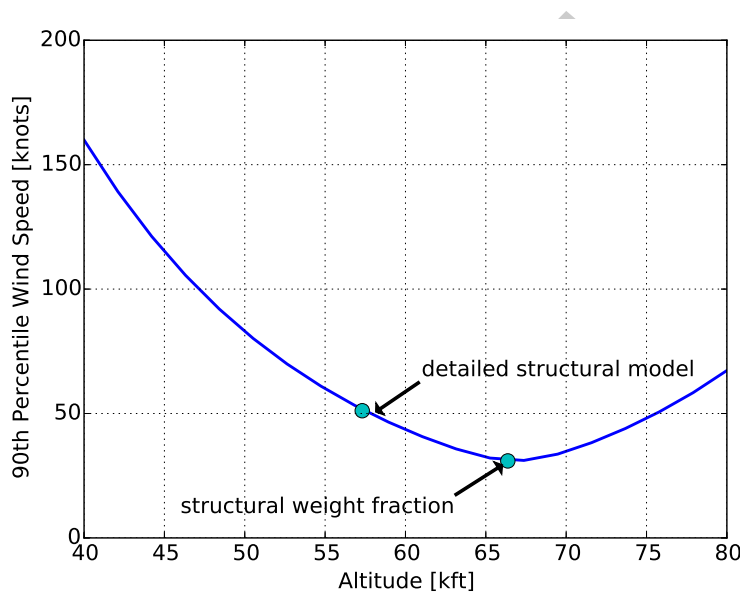


Figure 16: Comparison of simplified and detailed structural models highlights trade between wing weight and air density.

Another interesting result is the operating lift to drag ratio for the gas powered aircraft. The optimum lift to drag ratio to maximize endurance for gas powered aircraft is at the maximum $C_L^{1.5}/C_D$. [14] However, while station keeping, the aircraft will maintain a constant velocity during high wind speeds. At a constant velocity or constant Reynolds number the lift to drag ratio will not be at the maximum $C_L^{1.5}/C_D$. If it is assumed that wind speeds are negligible or that station-keeping is not important then velocity will be optimized such that the lift to drag ratio is at the maximum $C_L^{1.5}/C_D$ as shown in Figure 17.

D. Sensitivities

When a GP is solved, the sensitivity of the optimal objective value with respect to each constraint is also returned. From this information, the sensitivity of the optimal objective value to each fixed variable can be extracted. [8] While sensitivities are local and therefore only exact for small changes, they provide useful information about the relative importance of various design variables. For example, if the objective

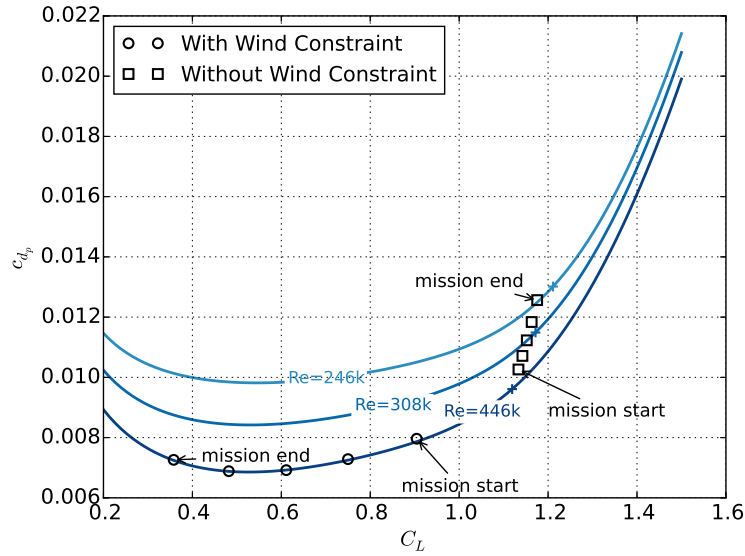


Figure 17: Wind speed constraint moves lift to drag ratio off maximum ($C_L^{1.5}/C_D$) point (plus signs). Solid lines are drag polars.

function were W_{MTO} and the sensitivity to battery specific energy were 0.5, then a 1% increase in the solar cell efficiency would result in a 0.5% increase in weight. Tables 3 and 4 show the variables with the highest sensitivities for the solar-electric and gas powered architectures respectively, where the objective was max take-off weight.

For the solar-electric aircraft, it is interesting to note that the battery discharge efficiency sensitivity is higher than the battery charge efficiency sensitivity. This occurs because the discharge efficiency directly affects the required battery size, whereas the charge efficiency only does so indirectly.

Table 3: Solar-Electric Powered Aircraft Sensitivities

Variable	25th Latitude	30th Latitude	25th Latitude	30th Latitude
	85th Percentile Winds	85th Percentile Winds	90th Percentile Winds	90th Percentile Winds
η_{prop}	-4.03	-4.42	-8.45	-14.4
$\eta_{discharge}$	-3.36	-3.68	-6.88	-11.6
t_{night}	3.16	3.46	6.5	11
h_{batt}	-2.59	-2.81	-4.79	-7.88
η_{solar}	-1.43	-1.59	-3.63	-6.45
$(E/S)_{irr}$	-1.26	-1.41	-3.34	-5.97
p_{wind}	1.17	1.97	3.49	8.59
η_{charge}	-0.774	-0.866	-2.09	-3.73
W_{pay}	0.732	0.727	0.798	0.974
ρ_{solar}	0.297	0.323	0.605	0.995

Table 4: Gas Powered Aircraft Sensitivities (90th Percentile Winds)

Variable	5 Day Endurance	7 Day Endurance	9 Day Endurance
V_{wind}	1.33	2.02	3.62
η_{prop}	-1.22	-1.89	-3.62
$BSFC_{\text{min}}$	1.19	1.84	3.51
t_{loiter}	1.17	1.82	3.49
W_{pay}	0.285	0.226	0.155
N_{max}	0.0706	0.123	0.302

VII. Conclusion

Using geometric programming as a means of evaluation of the design space, high level intuition and understanding about design trade studies for long-endurance aircraft and their driving requirements is achieved. One high level discovery is the importance of wind speed. If station keeping during any season or latitude is critical to the mission of a proposed aircraft, then that requirement is more likely to be met by a gas-powered architecture. However, if that constraint can be relaxed such that the aircraft only needs to station keep for 80% of the time, then for certain latitudes, a solar powered aircraft could achieve greater endurance. An unsurprising discovery is the sensitivity of the solar-powered aircraft to the battery specific energy and solar cell efficiency. Using higher energy density batteries can result in significant weight and performance savings. The rapid solve time of geometric programming is able to present these trade studies and give intuition into design trades by quantifying the disparity in performance between the two options.

VIII. Appendix

A. Discussion on the use of the *JH01* airfoil

The *sd7032* airfoil was redesigned to prevent drag creep by weakening the pressure spike associated with premature separation at higher Reynolds numbers. Figure 18 shows the pressure distributions generated in XFOIL of the *JH01* airfoil at $C_L = 0.0$ and $C_L = 1.35$ with $Re = 3 \times 10^5$. The redesigned airfoil was named *JH01*. We would like to thank Mark Drela for the redesign.

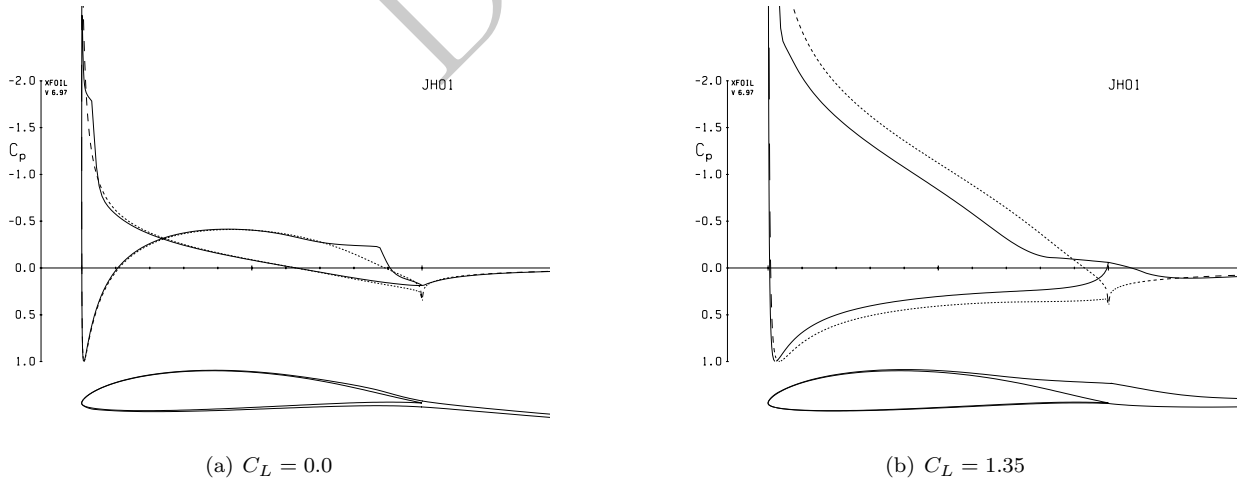


Figure 18: Pressure coefficient plots at the minimum and maximum expected C_L at Reynolds number $Re = 3 \times 10^5$.

B. Convex fitted functions

Some constraints in this optimization study are convex equations that approximate data or other functions. These equations include wind speed vs air density, airfoil drag polar, tail drag polar, BSFC to throttle mapping, and arctan equations. Each of these equations was generated using the fitting techniques described by Hoburg et. al.[12] All fitted equations are either *max-affine* or *softmax-affine* functions,

$$f_{\text{MA}}(\mathbf{x}) = \max_{k=1 \dots K} [b_k + \mathbf{x}_K^T \mathbf{x}] \quad (78)$$

$$f_{\text{SMA}}(\mathbf{x}) = \frac{1}{\alpha} \log \sum_{k=1}^K \exp(\alpha(b_k + \mathbf{a}_k^T \mathbf{x})). \quad (79)$$

The log-space RMS error,

$$\text{RMS error} \equiv \sqrt{\frac{1}{m} \sum_{i=1}^m (f(\mathbf{x}_i) - y_i)^2}, \quad (80)$$

is given throughout the paper for each equation, where m is the number of data points.

Bounds are imposed inside the optimization to ensure that the optimizer does not find a solution that exceeds the range over which the data was fitted. In the case of the wing and tail drag polar fitted equations, a post-solve process runs XFOIL and verifies that the optimized drag for a given lift coefficient and Reynolds number is within 5% of the XFOIL computed drag.

C. Solar energy calculations

The total available solar energy per day is an integral of the available solar power during the course of the day,

$$(E/S)_{\text{sun}} = \int_{t_{\text{sun rise}}}^{t_{\text{sun set}}} (P/S)_{\text{sun}} dt. \quad (81)$$

For simplicity, energy and power will refer to energy and power per unit area throughout the rest of this section (i.e. $(P/S) = P$). The solar irradiated power P_{sun} , is a function of θ , the angle between the normal to the flat surface, or aircraft wing, and the sun beam.[13]

$$P_{\text{sun}} = P_0 \cos \theta \quad (82)$$

The angle θ , depends on the time of day t , latitude ϕ , and declination angle Δ , [13]

$$\cos \theta = \sin \Delta \sin \phi + \cos \Delta \cos \phi \cos 2\pi t/24. \quad (83)$$

The declination angle Δ , can be found using the relation [13]

$$\begin{aligned} \Delta = & 0.006918 - 0.399912 \cos \beta + 0.070257 \sin \beta - 0.006758 \cos 2\beta + \\ & 0.000907 \sin 2\beta - 0.002697 \cos 3\beta + 0.00148 \sin 3\beta, \end{aligned} \quad (84)$$

where $\beta = 2\pi(\text{DOY} - 1)/365$. The time of day t_{day} , and the time of night t_{night} , can be calculated using a derivation of Equation (83), [13]

$$\cos(\pi t_{\text{sun rise}}/12) = -\tan \Delta \tan \phi \quad (85)$$

$$t_{\text{sun rise}} = -t_{\text{sun set}} \quad (86)$$

$$t_{\text{day}} = 2t_{\text{sun rise}} \quad (87)$$

$$t_{\text{night}} = 24 - t_{\text{day}} \quad (88)$$

where noon is $t = 0$. Both t_{day} and t_{night} affect the battery size as defined in Equations (52) and (53). The solar power available assuming no inclination angle P_0 , is found using the eccentricity of the earth's orbit,

$$P_0 = P_{\text{sun surface}} \frac{R_{\text{sun}}^2}{R_{\text{earth orbit}}^2}, \quad (89)$$

$$R_{\text{earth orbit}} = r_0 \left[1 + 0.017 \sin \left(2\pi \frac{\text{DOY} - 93}{365} \right) \right], \quad (90)$$

where

$P_{\text{sun surface}}$: Power emitted at the sun's surface
R_{sun}	: Radius of the sun
$R_{\text{earth orbit}}$: Distance from earth to sun
r_0	: Average distance from earth to sun
0.017	: Eccentricity of earth-sun orbit.

Using a trapezoidal integration of Equation (81), the total available solar energy per unit area can be obtained for a given latitude and day of the year. Because the equations in this appendix are not GP compatible, the total solar energy per unit area per day, the length of the day and the length of the night are calculated from the latitude and the day of the year prior to an optimization solve.

References

- ¹ Barr, Alistair; Albergotti, R., "Google to Buy Titan Aerospace as Web Giants Battle for Air Superiority," *Wall Street Journal*, 2014.
- ² Zuckerberg, M., "The technology behind Aquila," <https://www.facebook.com/notes/mark-zuckerberg/the-technology-behind-aquila/10153916136506634/>, jul 2016.
- ³ "Orion: Medium-Altitude Long-Endurance Unmanned Aircraft," http://www.aurora.aero/wp-content/uploads/2015/10/Orion-Brochure_web_X3.pdf.
- ⁴ Hatfield, D., Bale, P., and Barnes, P., "The VA001 aircraft," <http://www.vanillaaircraft.com/VA001.html>, 2016.
- ⁵ Boyd, S., S., K., L., V., and Hassibi, A., "A Tutorial on Geometric Programming," *Optimization and Engineering*, Vol. 8, No. 1, 2007, pp. 67–127.
- ⁶ G. Abbe, H. S., "Technological development trends in Solarpowered Aircraft Systems," *Renewable and Sustainable Energy Reviews*, Vol. 60, jul 2016, pp. 770–783.
- ⁷ Berrisford, P., Dee, D., Poli, P., Brugge, R., Fielding, K., Fuentes, M., Källberg, P., Kobayashi, S., Uppala, S., and Simmons, A., "The ERA-Interim archive Version 2.0," Shinfield Park, Reading, November 2011.
- ⁸ Hoburg, W., *Aircraft Design Optimization as a Geometric Program*, Ph.D. thesis, University of California, Berkeley, 2013.
- ⁹ Burnell, E. and Hoburg, W., "GPkit software for geometric programming," <https://github.com/hoburg/gpkit>, 2017, Version 0.5.2.
- ¹⁰ ApS, "The MOSEK C optimizer API manual," 2015, Version 7.1 (Revision 41).
- ¹¹ Burton, M., "Gas/Solar Trade," https://github.com/hoburg/gas_solar_trade, apr 2017.
- ¹² Warren Hoburg, P. K., "Data fitting with geometric-programming-compatible softmax functions," *Optimization and Engineering*, 2016.
- ¹³ McMordie, R. K., *Solar Energy Fundamentals*, The Fairmont Printing Press, Inc., 2012.

- ¹⁴ Lutze, F. H., “AOE 3104 Vehicle Performance,” <http://www.dept.aoe.vt.edu/lutze/AOE3104/range&endurance.pdf>.
- ¹⁵ Heckman, K., “Ellipsoid - Surface Area,” <https://www.vcalc.com/wiki/vCalc/Ellipsoid+-+Surface+Area>, nov 2016.
- ¹⁶ Supply, F., “Carbon and Kevlar Fabrics,” http://www.fiberglasssupply.com/Product_Catalog/Reinforcements/Carbon-and-Kevlar-Fabrics, may 2016.
- ¹⁷ Raymer, D. P., *Aircraft Design: A Conceptual Approach*, American Institute of Aeronautics and Astronautics, Inc., 4th ed., 2006.
- ¹⁸ Mauro Gatti, F. G., “Preliminary Design Analysis Methodology for Electric Multirotor,” *2nd IFAC Workshop on Research, Education and Development of Unmanned Aerial Systems*, Vol. 46, No. 30, nov 2013, pp. 58–63.
- ¹⁹ of North Dakota, U., “UAS Engines,” http://media.aero.und.edu/uasresearch.org/documents/195-197.Reference-Section_Engines.pdf.
- ²⁰ RCV Engines Ltd, E., “RCV DF35. 20x8 Zinger Prop. Static Operation,” private communication, apr 2016.
- ²¹ Goering, C. E., Stone, M. L., Smith, D. W., and Turnquist, P. K., *Off-Road Vehicle Engineering Principles*, chap. 2: Engine Performance Measures, American Society of Agricultural Engineers, 2003.
- ²² Hoover, A. L., “Density altitude and aircraft performance,” <https://yakimawpa.files.wordpress.com/2011/01/density-altitude-and-aircraft-performance-handout.pdf>.
- ²³ Drela, M., *XFOIL: An Analysis and Design System for Low Reynolds Number Airfoils*, Springer Berlin Heidelberg, Berlin, Heidelberg, 1989, pp. 1–12.
- ²⁴ Drela, M., “Wing Bending Calculations,” <https://ocw.mit.edu/courses/aeronautics-and-astronautics/16-01-unified-engineering-i-ii-iii-iv-fall-2005-spring-2006/systems-labs-06/spl10.pdf>.
- ²⁵ Duven, J. E., “Dynamic Gust Loads,” Advisory Circular 25.341-1, U.S. Department of Transportation, dec 2014.
- ²⁶ Clearwater Composites, L., “Properties of Carbon Fiber,” <http://www.clearwatercomposites.com/resources/Properties-of-carbon-fiber>, 2017.
- ²⁷ Drela, M., “Basic Aircraft Design Rules,” <https://ocw.mit.edu/courses/aeronautics-and-astronautics/16-01-unified-engineering-i-ii-iii-iv-fall-2005-spring-2006/systems-labs-06/spl8.pdf>, apr 2006.
- ²⁸ Cavcar, M., “The International Standard Atmosphere (ISA),” Anadolu University, 26470 Eskisehir, Turkey.
- ²⁹ Johnson, R. W., *The Handbook of Fluid Dynamics*, chap. Chapter 11, CRC Press, 1998.